# REPORT DOCUMENTATION PAGE

Form Approved OMB NO. 0704-0188



| 1. REPORT DATE (DD-MM-YYYY) | 2. REPORT TYPE | 3. DATES COVERED (From - To) |
|---|---|---|
| 30-05-2021 | Final Report | 25-Jul-2018 - 24-Jan-2021 |

**4. TITLE AND SUBTITLE**

Final Report: High-speed Cryogenics-enabling Electro-Optic Characterization System for Nanophotonic/Nanoelectronic Devices and Components

**5a. CONTRACT NUMBER**
W911NF-18-1-0391

**5b. GRANT NUMBER**

**5c. PROGRAM ELEMENT NUMBER**
611102

**6. AUTHORS**

**5d. PROJECT NUMBER**

**5e. TASK NUMBER**

**5f. WORK UNIT NUMBER**

**7. PERFORMING ORGANIZATION NAMES AND ADDRESSES**

University of California - San Diego
Office of Contract & Grant Adm
9500 Gilman drive, MC 0934
La Jolla, CA 92093 -0934

**8. PERFORMING ORGANIZATION REPORT NUMBER**

**9. SPONSORING/MONITORING AGENCY NAME(S) AND ADDRESS (ES)**

U.S. Army Research Office
P.O. Box 12211
Research Triangle Park, NC 27709-2211

**10. SPONSOR/MONITOR'S ACRONYM(S)**
ARO

**11. SPONSOR/MONITOR'S REPORT NUMBER(S)**
72232-EL-RI.11

**12. DISTRIBUTION AVAILIBILITY STATEMENT**

Approved for public release; distribution is unlimited.

**13. SUPPLEMENTARY NOTES**

The views, opinions and/or findings contained in this report are those of the author(s) and should not contrued as an official Department of the Army position, policy or decision, unless so designated by other documentation.

**14. ABSTRACT**

**15. SUBJECT TERMS**

| 16. SECURITY CLASSIFICATION OF: | | | 17. LIMITATION OF ABSTRACT | 15. NUMBER OF PAGES | 19a. NAME OF RESPONSIBLE PERSON |
|---|---|---|---|---|---|
| a. REPORT | b. ABSTRACT | c. THIS PAGE | | | Yeshaiahu Fainman |
| UU | UU | UU | UU | | 19b. TELEPHONE NUMBER 858-534-8909 |

# RPPR Final Report
as of 02-Jun-2021

Agency Code: 21XD

Proposal Number: 72232ELRI **Agreement Number: W911NF-18-1-0391**
**INVESTIGATOR(S):**


**Name:** Yeshaiahu Fainman
**Email:** fainman@ece.ucsd.edu
**Phone Number:** 8585348909
**Principal:** Y

Organization: **University of California - San Diego**
Address: Office of Contract & Grant Adm, La Jolla, CA 920930934
Country: USA

DUNS Number: 804355790 EIN: 956006144
**Report Date:** 24-Apr-2021 Date Received: 30-May-2021
**Final Report** for Period Beginning 25-Jul-2018 and Ending 24-Jan-2021
**Title:** High-speed Cryogenics-enabling Electro-Optic Characterization System for Nanophotonic/Nanoelectronic Devices and Components
**Begin Performance Period:** 25-Jul-2018 **End Performance Period:** 24-Jan-2021
**Report Term:** 0-Other

Submitted By: Yeshaiahu Fainman Email: fainman@ece.ucsd.edu
Phone: (858) 534-8909

**Distribution Statement:** 1-Approved for public release; distribution is unlimited.

**STEM Degrees:** **STEM Participants:**

**Major Goals:** The requested instrumentation will enable the generation of high-speed RF signals for characterization of the high-speed operation of ultra-fast nanolasers and high-speed adaptive receivers (HSARs) operating at regulated temperatures. Specifically, the requested equipment will facilitate research pertaining to (1) the design, fabrication and testing of ultra-fast tunable, intensity-modulated nanolasers and their arrays in a wide temperature range; (2) the design, fabrication and testing of fast tunable high-speed adaptive receivers and their arrays; and (3) the development of a novel setup with operation capabilities to characterize the nanolasers and high-speed adaptive receivers operating in pulsed regime (i.e. the data modulated regime) by exploiting the second-order intensity correlation technique.

**Accomplishments:** During the reporting period of this project, we conducted investigation of the modulation properties of proposed individual nanolasers and the temporal nonlinear dynamics of coupled nanolasers. We also demonstrated electro-optic switching in a novel CMOS compatible nonlinear material platform. In the attached document Section 1, we summarize our recent work in experimental demonstration of the wavelength tuning and intensity modulation properties of a single metallo-dielectric nanolaser. In Section 2, we present our further our study into coupled devices and present our recent progress in understanding the impact of the spontaneous emission factor ? on the dynamics and stabilities of coupled nanolasers. We show that high-? enhances the stability of coupled lasers, which states the importance of nanolasers with intrinsic large ? to be implemented in phase-locked laser arrays for high power and steerable beam generation. In Section 3, we present our progress in realizing lectro-optic switching in Silicon-Rich Nitride (SRN) waveguides by exploiting the third order nonlinear susceptibility, Chi(3). The extracted Chi(3) from our fabricated SRN film exceeds the highest index in literature that uses the same material platform. Our SRN waveguides also allows switching for both TE and TM electric fields for the same vertical field. Our work proves that SRN is a very promising material platform for a variety of on-chip applications.

# RPPR Final Report
as of 02-Jun-2021

**Training Opportunities:** The graduate and undergraduate students involved in this project obtain comprehensive research training in basic research, nanofabrication, characterization as well as testing system engineering. Their training includes developing rigorous electromagnetic, electronic and thermal modeling tools to design and analyze nanoscale semiconductor-metal-dielectric nanolasers and nonlinear optical composite metamaterials that possess enhanced nonlinear optical susceptibility for ultrafast switching. They also are trained in establishing the advanced tools and techniques required to fabricate these nanophotonic materials and devices, and use advanced characterization techniques such as measurements of electro-optic effect and nonlinear wave mixers. We recently constructed an apparatus for measurement of g2(?) as well as second order susceptibility in constructed metamaterials both in free space and guided wave geometries in a wide spectral range from visible to near infrared optical frequencies range. Our previous and current grant have contributed to the education and development of human resources in science and engineering at the postdoctoral, graduate, and undergraduate levels. We modified our undergraduate Photonics Instructional Laboratory by extending the experiment on computer holography, nonlinear optics and using soft lithography for rapid prototyping. The members of our group hold weekly technical meetings facilitating work in a team environment. Group members also hold weekly seminars where they make presentations on the progress of their work, new results in their research field, and other relevant science and technology topics. We also recruit undergraduate students to work in the lab through the NSF REU program. Their education will be enhanced by working alongside faculty, graduate students, and researchers in projects carried out by the faculty involved in this proposal as discussed above. To support K-12 education, we have continued developing modules for the California State Summer School for Mathematics and Science (COSMOS) program which brings high school students to the UCSD campus each summer. We will also further advance innovative education and outreach projects with the Preuss School and Sweetwater Union High School District, designed for students coming from disadvantaged households in grades 6-12 grades.

**Results Dissemination:** During the reporting period our group contributed to manuscripts in refereed journals and conference presentations. Further examples of data dissemination can be found at http://emerald.ucsd.edu. For this project we are using our past mechanisms for data dissemination.

**Honors and Awards:** Nothing to Report

**Protocol Activity Status:**

**Technology Transfer:** Technical interactions with Axalume on integration of RSOA with Si chips; linewidth characterization of the Si-photonic/RSOA lasers.

**PARTICIPANTS:**

**Participant Type:** PD/PI
**Participant:** Yeshaiahu Fainman
**Person Months Worked:** 1.00 **Funding Support:**
Project Contribution:
National Academy Member: N

**Participant Type:** Graduate Student (research assistant)
**Participant:** Suruj Deka
**Person Months Worked:** 3.00 **Funding Support:**
Project Contribution:
National Academy Member: N

**Participant Type:** Graduate Student (research assistant)
**Participant:** Sizhu Jiang
**Person Months Worked:** 3.00 **Funding Support:**
Project Contribution:
National Academy Member: N

# RPPR Final Report
as of 02-Jun-2021

**Participant Type:** Graduate Student (research assistant)
**Participant:** Athena Pan
**Person Months Worked:** 3.00 **Funding Support:**
Project Contribution:
National Academy Member: N

**Participant Type:** Graduate Student (research assistant)
**Participant:** Athena Pan
**Person Months Worked:** 3.00 **Funding Support:**
Project Contribution:
National Academy Member: N

**Partners**

,

I certify that the information in the report is complete and accurate:
Signature: Y. Fainman
Signature Date: 5/30/21 3:35PM

**2020 ARO report: Optoelectronic Technology for Nanosecond WDM-based Chip-scale Optical Networking, Y. Fainman – PI, UCSD**

During the reporting period of this project, we conducted investigation of the modulation properties of proposed individual nanolasers and the temporal nonlinear dynamics of coupled nanolasers. We also demonstrated electro-optic switching in a novel CMOS compatible nonlinear material platform. First, in Section 1, we summarize our recent work in experimental demonstration of the wavelength tuning and intensity modulation properties of a single metallo-dielectric nanolaser. In Section 2, we present our further our study into coupled devices and present our recent progress in understanding the impact of the spontaneous emission factor $\beta$ on the dynamics and stabilities of coupled nanolasers. We show that high-$\beta$ enhances the stability of coupled lasers, which states the importance of nanolasers with intrinsic large $\beta$ to be implemented in phase-locked laser arrays for high power and steerable beam generation. In Section 3, we present our progress in realizing electro-optic switching in Silicon-Rich Nitride (SRN) waveguides by exploiting the third order nonlinear susceptibility, $\chi^{(3)}$. The extracted $\chi^{(3)}$ from our fabricated SRN film exceeds the highest index in literature that uses the same material platform. Our SRN waveguides also allows switching for both TE and TM electric fields for the same vertical field. Our work proves that SRN is a very promising material platform for a variety of on-chip applications.

## 1. Wavelength Tunability and Intensity Modulation of a Metallo-dielectric Nanolaser

In this work, we report on simultaneously tuning the emission wavelength as well as altering the intensity of output light from a metallo-dielectric nanolaser. The mechanism is based on applying an external electric field to the nanolaser device which induces modifications in both the overlap of the electron and hole wavefunctions as well as the bound state energies via the quantum-confined Stark effect (QCSE).

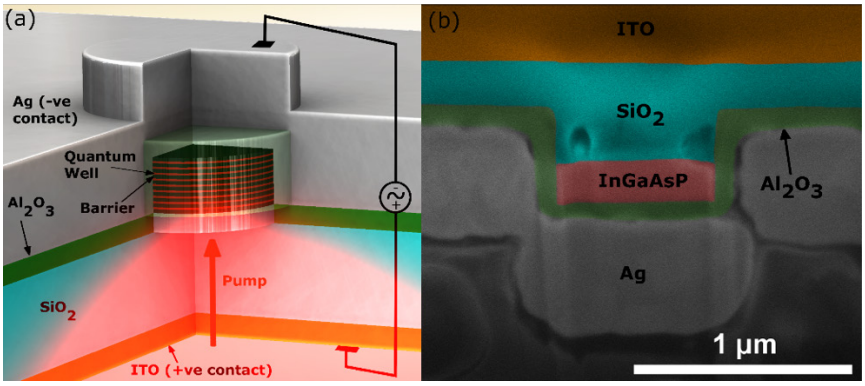


**Fig. 1:** (a) Device schematic of the metallo-dielectric nanolaser with constituent materials labelled. The gain comprises 10 nm thick InGaAsP quantum wells (shown in red) and 20 nm thick barriers (shown in black). The device is pumped from the bottom and emits in the same direction (shown via the red beam). The ITO thin film and Ag cladding serve as the bottom and top electrodes respectively, across which voltage is applied to the device (b) FIB cross-section image of a representative device with false color and constituent materials labelled.

The design and fabrication of the metallo-dielectric nanocavity used in this study builds onto the device first reported by Nezhad *et al.* [1] with modifications to enable external E-field to be applied to the device. Firstly, the gain in this work comprises of 300 nm of InGaAsP multiple quantum wells (MQWs) with wells and barriers of 10 and 20 nm thickness, respectively. Secondly, $Al_2O_3$ serves as the dielectric shield for the devices presented here instead of $SiO_2$ owing to better

thermal properties of the former [2]. In order to apply an electric field to tune/modulate the emission of the cavity, two additional fabrication steps were added as depicted in the device schematic in Fig. 1 (a). A layer of $SiO_2$ (~500 nm) was deposited to function as the insulator and then a thin film of ITO (~20 nm) was deposited on top of this dielectric layer and used as the bottom electrode. Although ITO is transparent at the NIR wavelengths of the nanolaser emission, it is still optically lossy and therefore, the film was chosen to be as thin as possible. Fig.1 (b) is an FIB cross-section image post-completion of all fabrication steps depicting a representative device with a gain radius of 455 nm.

### 1.1 Wavelength Tuning

In order to tune the nanolaser wavelength in real-time, an external electric field was applied perpendicular to the MQWs. A Cu substrate connected to the Ag-metal cladding was chosen as one electrode while the thin film of ITO functioned as the other. A voltage source (Keithley 2400) was then used to apply the voltage across the device while it was optically pumped at an input optical intensity of ~2*$P_{th}$, where $P_{th}$ denotes the device's lasing threshold intensity. The emitted output spectra of the nanolaser were subsequently recorded with a high-resolution monochromator. Fig. 2 (a) illustrates the results of applying varying amounts of DC voltage on a typical nanolaser device shown in Fig. 1 (a) and (b). To provide better intuition, values of the electric field are reported as voltage instead. From Fig. 2 (a), it can be observed that with increasing voltage, the nanolaser spectra are affected in two clear ways. First, the output intensity of the emitted light decreases monotonically till the emission is nearly suppressed at the highest values of the applied voltage. Secondly, the emission wavelength of the device redshifts, also monotonically, with increased voltage.

To better quantify these effects induced by the E-field, the nanolaser's peak output intensity, $P$, for each applied voltage is plotted in Fig. 2(b) as a percentage of the peak intensity, $P_0$, in the absence of the E-field/voltage. An almost linear drop in the peak output intensity can be observed with the attenuation in intensity as high as ~89% at the highest electric field/voltage value. Similarly, the alteration of the peak wavelength, $\Delta\lambda$, plotted on the right axis of Fig. 2 (b) is also significant and exhibits a redshift of around 8.35 nm with increased voltage. Redshifts in peak wavelength smaller than 150 pm can be achieved with only slight increments in the applied voltage (~0.65 V). This fine control also extends to the output intensity which can be attenuated by lower than ~2% as the voltage is varied. Such nuanced tuning of the emission along with the dynamical nature of the alterations themselves can prove to be invaluable if nanolasers are to be used for on-chip applications [3].

### 1.2 Intensity Modulation

For practical applications, high-speed modulation of nanolasers is desirable and in some cases such as for communication purposes, even imperative. To demonstrate the high-speed modulation capability of our devices under an external E-field, a small-signal modulation experiment was carried out where the device was pumped optically while an AC electric field was applied across the device's contacts. The output emission from the nanolaser was collected using a low-noise, high-gain APD (Thorlabs APD430C) which was then connected to an electrical spectrum analyzer (ESA, Keysight N9181A). If the device emission follows the AC signal of the voltage source, a peak would be registered in the ESA at the exact frequency of the AC input signal applied to the device via a function generator. Fig. 2 (c) illustrates the result of applying a 400 MHz sinusoidal AC voltage to the nanolaser which registers a clear AC signal amplitude on the ESA at the exact

frequency of the applied input signal. This confirms that our nanolaser can be modulated at a high speed of up to 400 MHz under external E-field modulation.

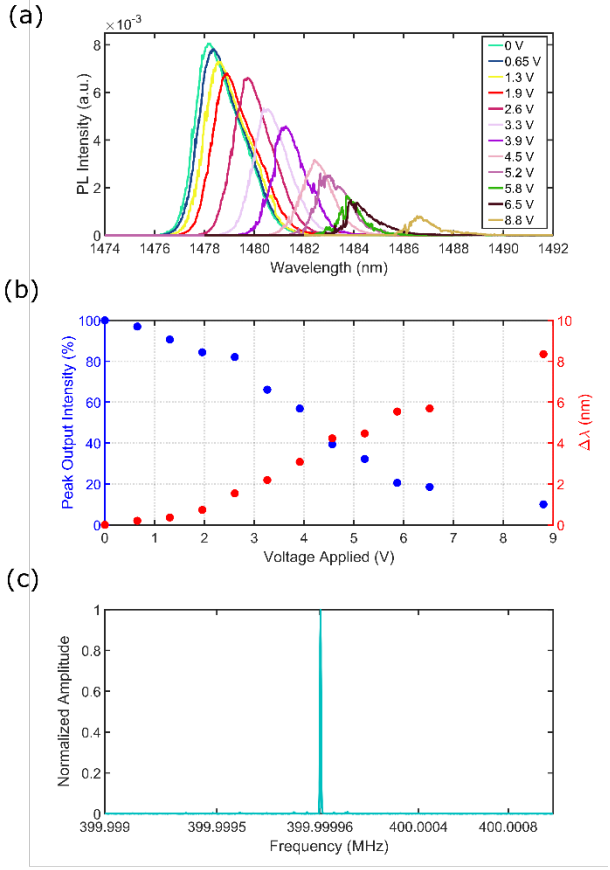


**Fig. 2:** (a) Real-time dynamic tuning of lasing wavelength by applying DC electric field/voltage across the device while pumping with an optical pulsed pump. (b) Peak output intensity percentage (blue) and change in peak wavelength - Δλ (red) – plotted as a function of the voltage applied to the device. The intensity is attenuated by ~89% and the wavelength is red shifted by ~8.35 nm when about 8.8 V is applied across the device. (c) 400 MHz modulation of the output intensity of the device as measured by a high-speed APD connected to an electrical spectrum analyzer. The span of the window is 2 kHz and the voltage applied is ~6.5 V.

Theoretically, emission alterations of nanolasers based on electronic effects can reach high speeds up to even the THz regime [4]. In practice, however, further demonstrations at higher modulation speeds were impeded by the response of the APD used in this study, which had a 3-dB bandwidth of 400 MHz. Nevertheless, as a proof-of-concept demonstration, the modulation speed at 400 MHz indicates that our modulation mechanism is due to electronic instead of thermal effects, the latter of which would have limited the upper modulation speed to the few megahertz regime [5]. Future efforts to attain high speeds in the gigahertz regime and beyond would involve altering the electrode design in order to minimize noise and realize planarized contacts more appropriate for handling high-speed signals. The manuscript based on the results presented in this section is accepted for publication [6].

## 2. Effects of High-$\beta$ on Phase-locking Stability in Coupled Nanolasers

Understanding the phase-locking stability and the nonlinear dynamics of coupled nanolasers becomes the natural step after individual devices are vastly investigated in both theories and

experiments. Phase-locked laser arrays are of great interest for their potential in generating high power optical beam as well as steerable coherent optical beams. Theoretical analysis of such laterally coupled lasers reported in the literature thus far have overlooked the effects of the spontaneous emission factor $\beta$. With the development of micro- and nanolasers with intrinsic high-$\beta$ factors over the past two decades, however, the impact of this parameter must be considered. In this work, we present the theoretical effects of varying $\beta$ on the stability of phase-locking, with varying pump rates and frequency detuning considered. The stable and unstable regimes of the coupled lasers are identified through a bifurcation analysis.

The coupled rate equations, with $\beta$ included, that govern the temporal dynamics two laterally coupled laser cavities considered here are given by:

$$\frac{d|E_{1,2}|}{d\tau} = \frac{1}{2}\left(\Gamma G(N_{1,2}) - \frac{1}{\tau_p}\right)|E_{1,2}| + \frac{\Gamma F_p \beta N_{1,2}}{2\tau_{rad}|E_{1,2}|^2}|E_{1,2}| \mp \kappa\cos(\Delta\Phi)|E_{2,1}| + \gamma\sin(\Delta\Phi)\,|E_{2,1}| \quad (1a)$$

$$\frac{dN_{1,2}}{d\tau} = P_{1,2} - \frac{N_{1,2}}{\tau_{nr}} - \frac{(F_p\beta + 1 - \beta)N_{1,2}}{\tau_{rad}} - G(N_{1,2})|E_{1,2}|^2 \quad (1b)$$

$$\frac{d\Delta\Phi}{d\tau} = \frac{\alpha}{2}\Gamma\big(G(N_2) - G(N_1)\big) + \Delta w + \kappa\left(\frac{|E_1|}{|E_2|} - \frac{|E_2|}{|E_1|}\right)cos(\Delta\Phi) - \gamma\left(\frac{|E_1|}{|E_2|} + \frac{|E_2|}{|E_1|}\right)sin(\Delta\Phi) \quad (1c)$$

where $|E_{1,2}|$ are the amplitudes of the electric fields in cavities 1 and 2, $|E_{1,2}|^2$ are the photon densities, $N_{1,2}$ are the carrier densities, $\Delta\Phi = \Phi_2 - \Phi_1$ is the phase difference between the two cavities, $\Delta w = w_2 - w_1$ is the frequency detuning between the cavities, $\alpha$ is the linewidth enhancement (Henry) factor, $\tau_p$ is the photon lifetime, $\tau_{rad}$ and $\tau_{nr}$ are the radiative and nonradiative lifetimes of the carriers, respectively, $\Gamma$ is the confinement factor, $F_p$ is the Purcell factor, $P_{1,2}$ are the pump rate, and $G(N_{1,2})$ are the carrier density-dependent gain functions. The coupling between two lasers are phenomenologically considered by introducing a complex coupling coefficient $i\kappa + \gamma$. $\kappa$ denotes the dispersive coupling that quantifies the frequency difference between two supermodes, and $\gamma$ denotes the dissipative coupling that quantifies the loss difference between the two supermodes.

### 2.1 Effects of $\beta$ on the stability conditions

The simplest representation of the model assumes zero frequency detuning $\Delta w = 0$, a constant pump rate $P_1 = P_2$, and a purely imaginary coupling coefficient, i.e. $\gamma = 0$. Fig. 3(a) and (b) illustrate the stability maps for in-phase and out-of-phase solutions, respectively, as a function of $\kappa$ and $\beta$; the variable $P_{th}$ denotes the pump power at lasing threshold for a single device. It can be observed in both figures that the stable phase-locking region grows as $\beta$ is increased from $10^{-5}$ to 1. Specifically, for the in-phase solutions shown in Fig. 3(a), it can be observed that increasing $\beta$ leads to a narrowing of the unstable region as the boundaries of the two Hopf bifurcations move towards each other. In fact, when $\beta = 0.89$, the two bifurcation branches become connected at $\kappa\tau_p \approx 0.09$ as shown in the inset of Fig. 3(a). For values of $\beta$ beyond this point of confluence (i.e. $\beta > 0.89$), the steady-state solutions of the rate equations yield in-phase, stable solutions irrespective of the coupling strength. This result holds major significance as it suggests that nanolasers with $\beta$ approaching 1 are ideal candidates to be used in phase-locking arrays to generate higher power. For example, $\beta = 0.25$ has been demonstrated in our previous work in metallo-dielectric nanolasers [7] as well as $\beta = 1$ in coaxial nanolasers [8].

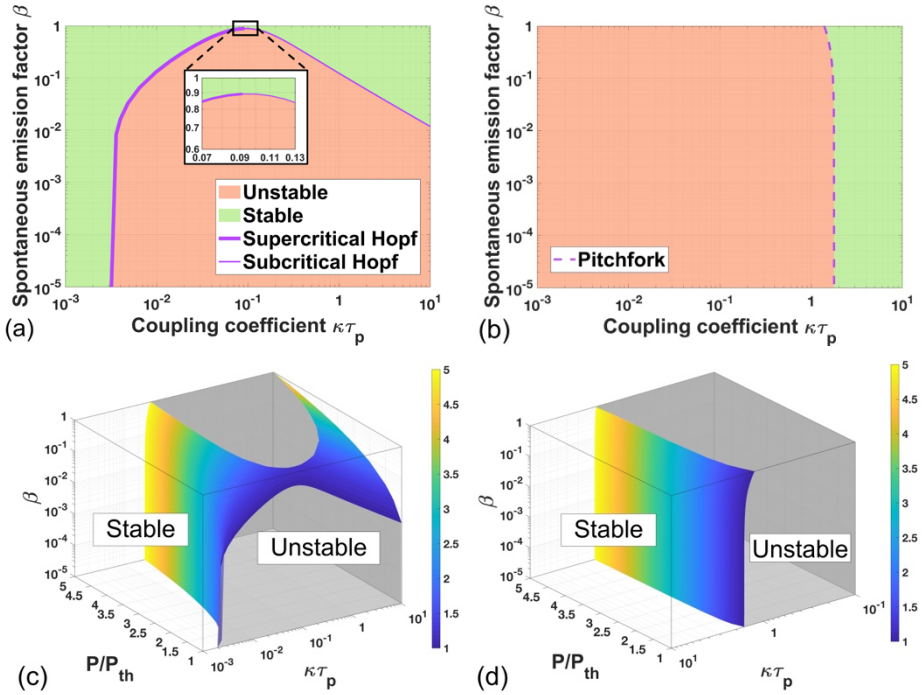


**Fig. 3:** 2-parameter bifurcation diagrams of the (a) in-phase solution and (b) out-of-phase solution in $(\kappa\tau_p, \beta)$ plane with $P_1 = P_2 = 1.2P_{th}$. Stable locking region is in green, unstable region is in orange. Purple lines are the supercritical (thick) and subcritical (thin) Hopf bifurcation boundary. Dashed line is the pitchfork bifurcation. (c) 3-dimensional stability plot in the $(\kappa\tau_p, P/P_{th}, \beta)$ plane for in-phase solutions. The 3-D surface is the Hopf bifurcation stability boundary. The color denotes various pump rate as shown in the colorbar. Stable phase locking region is in white, and the unstable region is in grey. (d) 3-D stability plot in the $(\kappa\tau_p, P/P_{th}, \beta)$ plane for out-of-phase solutions using same color convention as in (c).

### 2.2 Effects of pumping rate

In order to gauge whether increasing $\beta$ leads to a similar expansion in the stability regions when the pump rate is varied, 3-dimensional (3-d) stability plots for the in-phase and out-o-phase solutions are created as shown in Fig. 3(c) and (d), respectively. Despite the complex shape of the surface in Fig. 3(c), which is the Hopf bifurcation stability boundary, higher $\beta$ values always contribute towards increased in-phase locking for arbitrary pumping rate $P/P_{th} \in [1,5]$. A varying pump rate has negligible effect on the stability of out-of-phase solutions, as seen in Fig. 3(d).

### 2.3 Effects of frequency detuning

In practice, slight dissimilarities in the dimensions of the resonators can easily result due to fabrication imperfections, which consequentially yield disparate resonance frequencies. Therefore, it is imperative to investigate whether the advantageous characteristics of high-$\beta$ with regards to stability hold true even when the frequencies of the two lasers are detuned relative to each other. We focus our analysis on the in-phase solution as it is more interesting for most applications. The stability plot in 3-d parameter space $(\kappa\tau_p, \Delta w\tau_p, \beta)$ are derived from the bifurcation analysis and are further divided into $\kappa\tau_p \in [10^{-3}, 0.1]$ in Fig. 4(a) and $\kappa\tau_p \in [0.1,200]$ in Fig. 4(b) for better visualization. Detuning of the frequencies give rise to two symmetric saddle-node (SN) bifurcation boundaries, that enclose the in-phase stable locking region together with the Hopf bifurcation

boundary when $\kappa\tau_p < 0.1$. It can be observed that, as $\beta$ increases, although the SN boundaries remain largely unperturbed, the supercritical Hopf branch relocates to higher $\kappa\tau_p$ values. This, in return, expands the stable locking region for weak coupling ($\kappa\tau_p < 0.1$). For strong coupling regime in Fig. 4(b), where $\kappa\tau_p > 0.1$, the second stable phase locking region is solely determined by another Hopf boundary, which shifts towards smaller $\kappa\tau_p$ for higher $\beta$, thereby increasing the area of stable phase locking. The results here indicate that increasing $\beta$ expands the stability regions in both weak and strong coupling cases, despite the lasers demonstrating dissimilar frequencies. Such effect becomes even more significant for $\beta$ exceeding 0.1. Therefore, nanolasers with intrinsic high $\beta$ values have great potential to be implemented in laser arrays, where shifted frequencies between adjacent elements are required to build ultra-high-resolution lidar systems for distance-angle beam steering tasks [9].

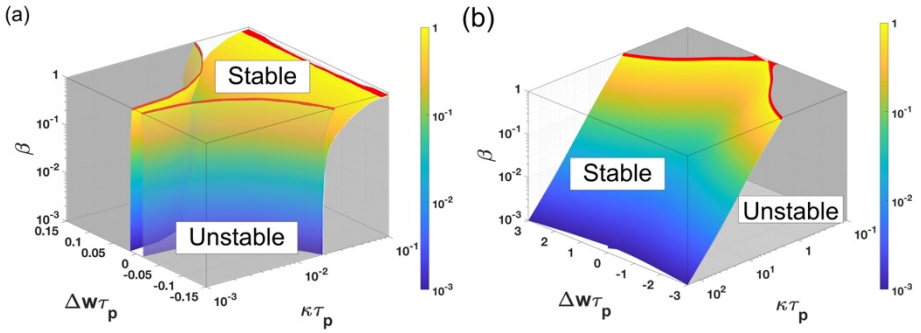


**Fig. 4:** (a) 3-dimensional stability plot in the $(\kappa\tau_p, \Delta w\tau_p, \beta)$ plane for in-phase solutions with $\kappa\tau_p \in [10^{-3}, 10^{-1}]$. The 3-D surfaces are the stability boundaries for Hopf and SN bifurcations. The colors denote varying $\beta$ as shown in the colorbar. The red region denotes $\beta \geq 0.89$. Stable phase locking region is shown in white, and the unstable region is colored in grey. (b) 3-D stability plot in the $(\kappa\tau_p, \Delta w\tau_p, \beta)$ plane for in-phase solutions with $\kappa\tau_p \in [10^{-1}, 200]$ using the identical color convention as in (b).

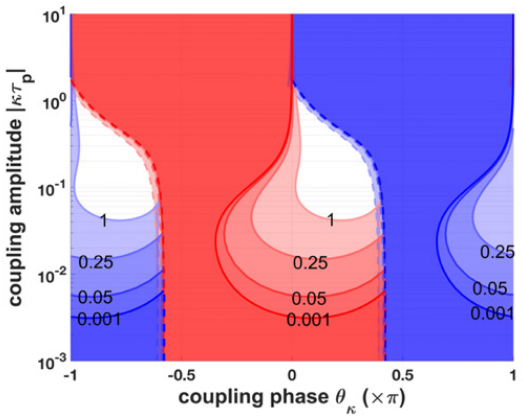


**Fig. 5:** 2-parameter bifurcation diagrams of in-phase and out-of-phase solutions in the $(|\kappa\tau_p|, \theta_\kappa)$ plane with $\beta = 10^{-3}, 0.05, 0.25$ and 1. The stable in-phase locking region is shown in red; the stable out-of-phase locking region is colored in blue and the unstable region is shown in white. The solid lines denote Hopf bifurcations, while the dashed lines denote Pitchfork bifurcations.

To further extend our theoretical model to cover various coupling platforms, it is necessary to consider the dissipative coupling coefficient $\gamma$ due to the loss difference between the supermodes arising from the coupling. To simplify the ensuring bifurcation analysis, instead of simply using $\kappa$ and $\gamma$, the coupling amplitude and phase are used by setting $i|\kappa|e^{j\theta_\kappa} = i\kappa + \gamma$, where $\theta_\kappa \in$

$[-\pi, \pi]$. Frequency detuning between coupled lasers is neglected for simplicity. Fig. 5(a) presents the stability plots for $\beta = 10^{-3}$, 0.05, 0.25 and 1 while considering complex coupling coefficient. It can be observed that the stability regions of in-phase (red) and out-of-phase (blue) with the same $\beta$ values are identical in shape albeit shifted with respect to each other by $\pi$ radians. The more significant finding from the figure is that as $\beta$ increases, both the in-phase and out-of-phase solutions expand in size for the complex coupling coefficient model considered here.

In summary, with regards to stable phase-locking, increasing $\beta$ unequivocally leads to an expansion in the stability regions despite considering varying pump rates, detuned resonance frequencies and both purely imaginary and complex coupling coefficients. The robustness of the desirable effects of high- $\beta$ on stability truly emphasize the tantalizing potential that nanolasers, that harness this advantage, demonstrate in being used for developing next generation high-power laser arrays and optical phased arrays. The manuscript that summarizes this presented work is currently under preparation [10]. As a continuation of this theoretical work, we are working on the design, fabrication and demonstration of two coupled nanolasers locking in-phase.

## 3. Optical Nonlinearities for Switching

### 3.1 Effective Second Order Nonlinearities – The DC-Induced Pockels effect

In continuation of our work exploring novel platforms for energy efficiency, low-cost optical switching we have focused our efforts expanding upon our work on the DC-Induced Pockels effect. Previously we have demonstrated the electric field induced second harmonic effect (EFISH) [11] for developing effective second order nonlinearities in second harmonic generation in a thin film silicon rich nitride platform. We then showed initial results using the DC-Induced Pockels effect for developing effective second order nonlinearities for in-waveguide switching. In continuation of this on-going work we continue to fully explore silicon-rich nitride as a platform for optical switching using effective second order nonlinearities through the DC-Induced Pockels effect.

As previously, it is helpful to begin from an expansion of the polarizability. Shown below in equation 2.1 is an expansion of the nonlinear portion of the polarizability including up to the third order terms.

$$\begin{aligned}\bar{P}_{NL} &= \epsilon_0\{\underbrace{\chi^{(2)}\left[2EE^* + E_{dc}^2\right]}_{\text{Electrostatic}} + \underbrace{\chi^{(2)}\left[2E_{dc}Ee^{-j\omega t} + 2E_{dc}E^*e^{j\omega t}\right]}_{\text{Pockels}} + \underbrace{\chi^{(2)}\left[E^2e^{-j2\omega t} + E^{*2}e^{j2\omega t}\right]}_{\text{SHG}} + \underbrace{\chi^{(3)}\left[E_{dc}^3 + 6EE^*E_{dc}\right]}_{\text{Electrostatic}} \\ &+ \underbrace{\chi^{(3)}\left[\left(3E_{dc}^2E + 3E^2E^*\right)e^{-j\omega t} + \left(3E_{dc}^2E^* + 3EE^{*2}\right)e^{j\omega t}\right]}_{\text{Kerr effect and DC-Induced Pockels}} + \underbrace{\chi^{(3)}\left[3E_{dc}E^2e^{-j2\omega t} + 3E_{dc}E^{*2}e^{j2\omega t}\right]}_{\text{EFISH}} + \underbrace{\chi^{(3)}\left[E^3e^{-j3\omega t} + E^{*3}e^{j3\omega t}\right]}_{\text{THG}}\}\end{aligned}$$

**Equation 2.1:** An expansion of the nonlinear portion of the polarizability out to the third order contributions. Take special note of how the EFISH term is a third order nonlinearity but contributions to the second harmonic term and compare this to the similar between the Kerr and DC-Induced Pockels effect and the Pockels Effect.

If we take the DC-Induced Pockels terms and relate them to an effective linear susceptibility we can derive equation 2.2(a) below for the change in refractive index ($\Delta n_i$) based on an applied electric field. It is important to note that for silicon-rich nitride's material class only certain tensor components can be non-zero. Therefore, to uniquely attribute our experiment to the two contributing tensor components separately we will impose some field and symmetry conditions based on our electrode design in order to simplify equation 2.2(a) into equation 2.2(b)

$$(\boldsymbol{a}):\ \Delta n_i = \frac{3\,\Gamma_{SRN}}{2}\sum_{j,k,l}\frac{\chi^{(3)}_{ijkl}}{n_{l,eq}}E^{dc}_j E^{dc}_k \qquad (\boldsymbol{b}):\ \Delta n_i = \frac{3\,\Gamma_{SRN}}{2}\sum_{i,j}\frac{\chi^{(3)}_{ijji}}{n_{i,eq}}E^{dc^2}_j$$

**Equation 2.2:** (a) The generic form of the induced change in refractive index for an applied field with components along $\hat{j}$ and $\hat{k}$ based on the DC-Induced Pockels Effect. (b) Reduced form based on symmetry and imposed field conditions.

Our electrode design is very important for this study as we wish to be able to uniquely attribute our measurements to the two contributing tensor components separately. In order to properly model the applied field distribution, capacitance versus voltage and current versus voltage measurements where performed in order to determine the RF permittivity and breakdown field of our silicon-rich nitride thin films. From these measurements, shown below, we determined the RF permittivity to be 9.0578 and the breakdown field to be greater than 1.2E8 v/m post annealing.

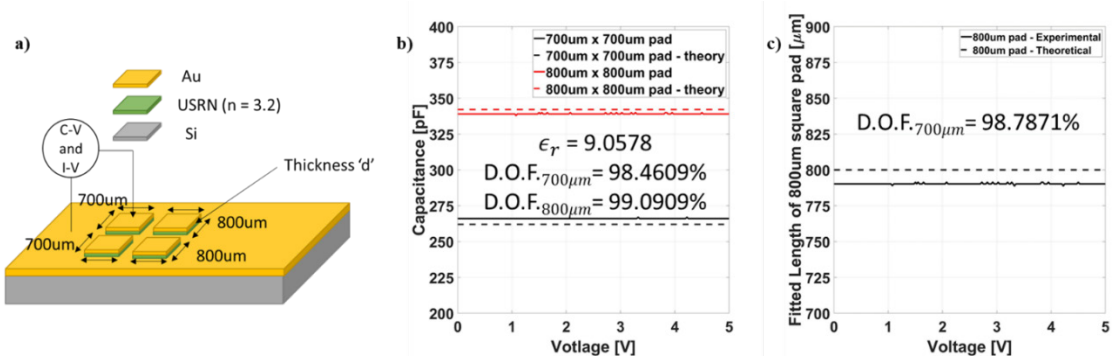


**Fig. 6:** (a) Schematic breakdown of the test structure used to extract the RF permittivity. Capacitance vs voltage measurements are performed using an Agilent B1500A semiconductor device analyzer. Thickness 'd' = 150nm. (b) Capacitance [pF] vs Voltage [V] at 100 kHz along with a fitting for the relative permittivity showing a value of 9.0578. (c) Confirmation of the fitting where the effective length [$\mu$m] of one pad is extracted based on fitting the other pad for its relative permittivity. As can be seen the fitting is good using either method and show similar results.

Using this we designed the electrode configuration, shown below in Fig. 7(a)+(c), to maximize the difference between the in-plane and out-of-plane components of the applied field achieving a 3 order of magnitude difference. We then chose to utilize this electrode design in a racetrack ring resonator, placing 220um long electrodes in each of the two 250um long straight sections of the racetrack ring, see Fig. 7(a).

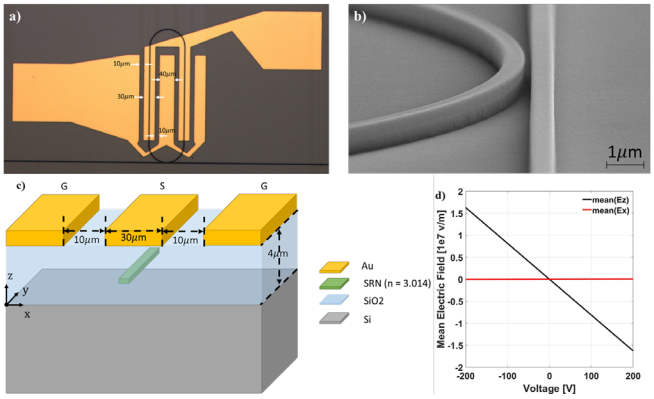


**Fig. 7:** (a) Optical microscope image of our point coupled micro-ring resonator with electrode width and spacing marked with white arrows and text overlay. (b) Scanning Electron Microscope image

of the point coupler region. (c) Schematic breakdown of the phase shifter design shown as a cutout. (d) Plot of the mean value of the Applied Field $E_x$ and $E_z$ components versus voltage inside the waveguide core.

The design of our electrodes, and the decision to utilize a racetrack ring resonator allows us to uniquely attribute electro-optic measurements of the TE- and TM- polarized optical modes to the tensor components $\chi^{(3)}_{1331}$ and $\chi^{(3)}_{3333}$ respectively. This is the importance of the electrode design as these two tensors being the only two contributing non-zero tensors allows us to give a proper tensorial treatment of the DC-Induced Pockels effect using our measurements of these racetrack ring resonators operating in TE- and TM- modes.

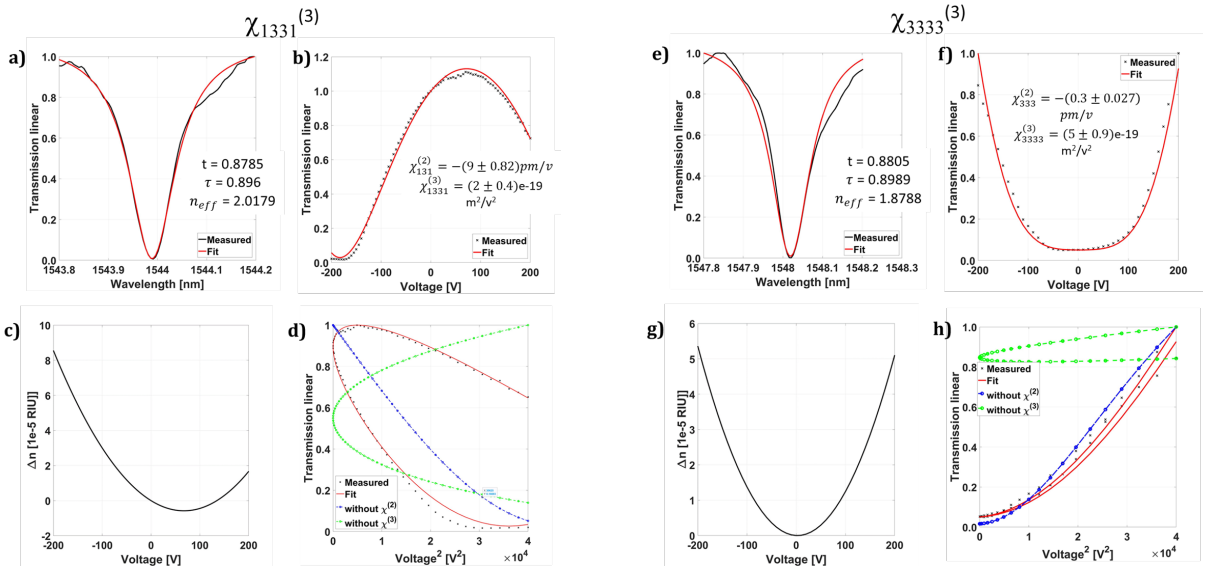


**Fig. 8:** (a)-(d), (e)-(h) Measurements of transmission versus wavelength and transmission versus applied voltage for the case of the TE- and TM- polarized optical modes respectively. (a) Plot of transmission versus wavelength for one resonance of TE- polarized optical mode fit for t, $\tau$, and effective refractive index. (b) Plot of transmission versus applied voltage operating at a fixed wavelength of 1544.02 nm in the TE- polarized optical mode case normalized to the transmission at 0 volts applied and fit for $\chi^{(2)}_{131}$ and $\chi^{(3)}_{1331}$ as well as the overlap factor. (c) Plot of the extracted change in effective refractive index versus applied voltage for the TE case (d) Plot of transmission versus applied voltage squared at a fixed wavelength of 1544.02 nm in the TE- polarized optical mode case normalized to the maximum transmission. (e) Plot of transmission versus wavelength for one resonance of the TM- polarized optical mode fit for t, $\tau$, and effective refractive index. (f) Plot of transmission versus applied voltage operating at a fixed wavelength of 1548.02 nm in the TM- polarized optical mode case normalized to the maximum transmission and fit for $\chi^{(2)}_{333}$ and $\chi^{(3)}_{3333}$ (g) Plot of change in effective refractive index versus applied voltage for the TM case extracted from (f). (h) Plot of transmission versus applied voltage squared at a fixed wavelength of 1548.02 nm in the TM- polarized optical mode case normalized to the maximum transmission.

For characterization, we use a combination of optical and electro-optic measurements to fully extract the material parameters of interest and in doing so demonstrate electro-optic switching based on the quadratic electro-optic effect. We use a fiber coupled input and a free-space output setup with a tunable Agilent 8164B CW source with a wavelength span of 1465nm to 1575nm [11]. Electrical probes are used to contact the electrode pads (see Fig. 7(a)) applying voltage from a Keithly SourceMeter 2400 with a maximum voltage range of $\pm$210V with the sample placed on a thermally controlled stage. Note that although this range may seem large the actual field within

the waveguide core is 1.6E7 v/m at 200 volts, and that due to the electrode design, as discussed below, large voltages are needed to achieve these field strengths. Note, that more optimized electrode design will significantly reduce the required voltage to few volts.

Two measurements are performed in our experimental characterization: we first measure the passive transmission spectra of our racetrack resonators, followed by a second measurement of the transmission spectra as a function of the applied voltage at a fixed wavelength. These two measurements are repeated for TE- and TM- polarizations. Fig. 8(a) – (d) and Fig. 8(e) – (h) show the measured results for the TE- and TM- polarizations, respectively. We achieve a maximum extinction ratio of ~16dB and ~13dB for the TE and TM cases, respectively. In both cases, the transmission versus wavelength results are first fit to extract the self-coupling coefficient, t, the single pass retention factor, $\tau$ ,and the effective refractive index in accordance with [12,13], the results of which can be seen in Fig. 8(a) and (e). These parameters are then used to fit for the $\chi^{(2)}$ and $\chi^{(3)}$ by fitting for the change in effective refractive index as a function of applied field utilizing Lumerical Mode Simulations to solve for the effective refractive as a function of change in material index, which is in turn derived from modelling of the applied field within the waveguide in Lumerical Device. The results of a best fit optimization can be seen in Fig. 8(b) and (f). Corresponding change in effective refractive index can be seen in Fig. 8(c) and (g).

In this work we present and discuss ongoing results of a low-loss PECVD silicon-rich nitride film with a refractive index of 3.0 or higher and use it to undertake a systematic evaluation of the DC-induced Pockels effect or electro-optic switching. Further optimization of the electrode design is needed to maximize field strength rather than linearity as shown here; however, electro-optic switching in silicon-rich nitride is a promising avenue of exploration for a low-cost energy efficient optical switch.

## References


[1] M. P. Nezhad, A. Simic, O. Bondarenko, B. Slutsky, A. Mizrahi, L. Feng, Vitaliy Lomakin, and Y. Fainman. "Room-temperature subwavelength metallo-dielectric lasers." *Nature Photonics 4*, no. 6 (2010): 395-399.

[2] Q. Gu, J. Shane, F. Vallini, B. Wingad, J.S.T. Smalley, N.C. Frateschi, and Y. Fainman. "Amorphous $Al_2O_3$ shield for thermal management in electrically pumped metallo-dielectric nanolasers." *IEEE Journal of Quantum Electronics 50*, no. 7 (2014): 499-509.

[3] R.M. Ma, and R.F. Oulton. "Applications of nanolasers." *Nature Nanotechnology 14*, no. 1 (2019): 12-22.

[4] D.A.B. Miller. "Device requirements for optical interconnects to silicon chips." *Proceedings of the IEEE 97*, no. 7 (2009): 1166-1185.

[5] D. Massoubre, J.L. Oudar, A. O'Hare, M. Gay, L. Bramerie, J.C. Simon, A. Shen, and J. Decobert. "Analysis of thermal limitations in high-speed microcavity saturable absorber all-optical switching gates." *Journal of lightwave technology 24*, no. 9 (2006): 3400.

[6] S. S. Deka, S. H. Pan, S. Jiang, A. El Amili, F. Vallini, Q. Gu and Y. Fainman, "Real-Time Dynamic Wavelength Tuning and Intensity Modulation in Metal-Clad Nanolasers," *manuscript accepted for publication.*

[7] S. H. Pan, Q. Gu, A.E. Amili, F. Vallini, and Y. Fainman, "Dynamic hysteresis in a coherent high-β nanolaser." *Optica 3*, no. 11 (2016): 1260-1265.

[8] M. Khajavikhan, A. Simic, M. Katz, J. H. Lee, B. Slutsky, A. Mizrahi, V. Lomakin, and Y. Fainman. "Thresholdless nanoscale coaxial lasers." *Nature 482*, no. 7384 (2012): 204-207.
[9] P. Antonik, M.C. Wicks, H.D. Griffiths, and C.J. Baker. "Frequency diverse array radars." *In 2006 IEEE Conference on Radar*, pp. 3. IEEE, 2006.
[10] S. Jiang. S.S. Deka, S.H. Pan, and Y. Fainman. "Effects of high-$\beta$ on phase-locking stability and tunability in laterally coupled lasers", manuscript in preparation.
[11] Lin, Hung-Hsi, Rajat Sharma, Alex Friedman, Benjamin M. Cromey, Felipe Vallini, Matthew W. Puckett, Khanh Kieu, and Yeshaiahu Fainman. "On the observation of dispersion in tunable second-order nonlinearities of silicon-rich nitride thin films." *APL Photonics* 4, no. 3 (2019): 036101.1
[12] R. Sharma, M. W. Puckett, H. Lin, A. Isichenko, F. Vallini, and Y. Fainman, *Opt. Lett.* 41, 1185 (2016).
[13] W. Bogaerts, P. D. Heyn, T. V. Vaerenbergh, K. D. Vos, S. K. Selvaraja, T. Claes, P. Dumon, P. Bienstman, D. V. Thourhout, and R. Baets, *Laser & Photonics Reviews*, 6, 47 (2012).
[14] A. Friedman, H. Neejadriahi, R. Sharma, and Y. Fainman. "A demonstration of Electro-optic Switching in Silicon-Rich Silicon Nitride" *manuscript xxxxxxxxxxx.*